CRYSTAL GROWTH & DESIGN

pubs.acs.org/crystal

Article

Second Harmonic Generation Behavior of Two New D-Ribose/D-Fructose and Metal Halogenide-Based Coordination Compounds and Comparison to D-Fructose and D-Galactose Analogues: An Experimental and Theoretical Approach

Domenica Marabello,* Paola Antoniotti, Paola Benzi, Carlo Canepa, Elena Cariati, Alma Cioci, and Leonardo Lo Presti

Cite This: *Cryst. Growth Des.* 2022, 22, 5923−5934

Read Online

ACCESS | Metrics & More | Article Recommendations | Supporting Information

ABSTRACT: This work is focused on the understanding of the second harmonic generation (SHG) behavior of metal halogenides−saccharide-based compounds. Three new compounds were added to a list of such compounds that were previously analyzed by our group in order to deepen the understanding of the relationship between the SHG behavior of these materials and their structural and/or chemical properties. These new compounds were the object of theoretical calculations with two different computational approaches (nanoparticle and bulk) and were characterized by single-crystal X-ray diffraction (XRD), and SHG measurements were performed. The results demonstrate that DFT simulations can be considered as reliable predictors of the order of magnitude of the experimental measures. The nanoparticle calculations take into account the finite size of the crystals in the powders and the lowering of symmetry due to their defects. A multivariate analysis is performed to elucidate the relationship between the structural, chemical, and physical parameters and the NLO response.

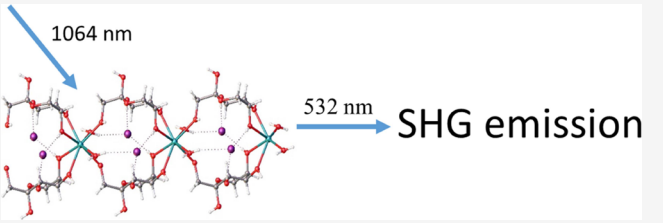

■ INTRODUCTION

In the last few decades, the interest on biocompatible materials increased because of the possibility to detect nanoparticles of these materials in biological systems. For these biosensing applications, materials with second harmonic generation (SHG) properties are particularly relevant because SHG nanoprobes show many advantages with respect to the fluorescence compounds.[1−5] Even if the SHG phenomenon has been known for years,[6] the relationship between the SHG behavior of a material and its structural and/or chemical properties is not completely clarified: the only certainty in the field of crystals is that the SHG is a second-order nonlinear optical effect that occurs in noncentrosymmetric crystals.[7]

For many years, our research has been focused on saccharide-derived metal−organic frameworks (MOFs) with SHG properties and their potential applications as biosensors because of their high biocompatibility, the lack of inversion symmetry in the crystal structures that induces the SHG properties, and their capability to complex metal cations and pull polarizable anions into the structure. Several $M(sugar)_nX_2$ complexes (M = Ca, Sr; sugar = D-fructose, 2-deoxy-D-galactose; X = Cl, Br, I) were synthesized, and their SHG behavior was experimentally and theoretically studied. In particular, we studied the influence of different cations and/or anions and/or sugar and/or of their different spatial disposition in the crystals on the SHG behavior. In order to deepen this investigation, in the present work, we analyzed three new compounds, two composed of D-ribose and calcium bromide or strontium bromide and one based on D-fructose and calcium iodide. By combining D-ribose with MBr_2 (M = Ca, Sr), we obtained two new isomorphous molecular compounds of formula $[M(C_5H_{10}O_5)_2]Br_2$, hereafter, CaRIBBr and SrRIBBr, respectively. From fructose and CaI_2, we obtained the MOFs of formula $[Ca(C_6H_{12}O_6)_2(H_2O)_2]I_2$, CaFRUI.

The three compounds were characterized by single-crystal X-ray diffraction (XRD), and experimental SHG measurements on powders were performed. In order to better correlate the second harmonic emission with the nature and structure of the materials, also theoretical calculations were carried out with two different computational approaches: a model in which the crystalline fragment is represented as a nanoparticle (nanoparticle calculations) and a model in which the crystal is infinite and perfect (bulk calculations). These two approaches represent the two extremes in which the real crystalline

Received: May 17, 2022
Revised: August 18, 2022
Published: August 30, 2022

https://doi.org/10.1021/acs.cgd.2c00560
Cryst. Growth Des. 2022, 22, 5923−5934

powders lie. In both cases, the geometrical parameters were optimized and compared with the experimental XRD data; the first-order static hyperpolarizability and second-order susceptibility were also calculated and compared with the values obtained for the sucrose used as a reference. These results were compared with the experimentally measured SHG intensity ratios.

The aim of this study is an attempt to understand which crystals' or chemical feature plays a role on the SHG response of these complexes. For this purpose, further experimental measurements and parallel computational calculations were performed on the compounds previously studied to standardize the analysis and to allow a comparison of the SHG behaviors of all the studied complexes.

■ EXPERIMENTAL SECTION

Synthesis of $[Ca(C_5H_{10}O_5)_2(H_2O)_3]Br_2$ (CaRIBBr) and $[Sr(C_5H_{10}O_5)_2(H_2O)_3]Br_2$ (SrRIBBr). Calcium or strontium bromide and D-ribose powders were mixed in stoichiometric ratios 2:1, 1:1, and 1:2, and ground in an agate mortar. During the grinding in the agate mortar, due also to the air humidity, the reagents start to combine in both cases as proven by the formation of sticky materials. The XRD patterns revealed the amorphous nature of the materials, and only the partial dissolution in ethanol allowed their crystallization. The solids obtained were partially dissolved in a few drops of ethanol, and the solutions were maintained at equilibrium with the solid for a week. Colorless crystals, suitable for the XRD analysis, were formed on the walls of the vial of the 1:1 (Ca) and 1:2 (Sr) solutions. They were washed quickly with a few drops of ethanol and dried in an oven at 323 K. To avoid the absorption of humidity during the X-ray measurements, the mounted crystals were covered with paraffin oil.

Synthesis of $[Ca(C_6H_{12}O_6)_2(H_2O)_2]I_2$ (CaFRUI). Calcium iodide and β-D-fructose powders were mixed in stoichiometric ratios 2:1, 1:1, and 1:2 and ground in an agate mortar. As for the MRIBBr salts, the reagents start to combine during grinding. The sticky solids obtained was dissolved in a few drops of ethanol, and the solution was evaporated in an oven at 323 K. After a few days, molasses is formed that crystallizes completely after further heating in about two weeks. The colorless crystals were washed quickly with a few drops of ethanol and dried in an oven at 323 K. Crystals suitable for the XRD technique were extracted from the molasses obtained from the 1:2 stoichiometric solution and covered with paraffin oil to avoid the absorption of humidity during the X-ray measurements.

Single-Crystal XRD. XRD data for CaRIBBr and SrRIBBr were collected at room temperature using an Oxford Diffraction Gemini R Ultra diffractometer. Data were collected with graphite monochromatized Mo-Kα radiation (0.71073 Å). The CrysAlisPro[8] package was used for data collection and integration, SHELXT[9] for resolution, SHELXL[10] for refinement, and Olex2[11] for graphics.

Crystal data for CaRIBBr (M = 554.21 g/mol): monoclinic, space group C2, Z = 2, a = 17.315(4) Å, b = 6.5666(6) Å, c = 12.909(3) Å, β = 137.89(4), V = 984.3(6) Å^3, 5279 reflections collected of which 2191 unique (R_{int} = 0.0445). R_1 = 0.0463 ($I > 2\sigma(I)$), wR_2 = 0.1106 (all data).

Crystal data for SrRIBBr (M = 600.74 g/mol): monoclinic, space group C2, Z = 2, a = 17.206(1) Å, b = 6.7707(4) Å, c = 11.6873(7) Å, β = 132.358(5)°, V = 1006.1(1) Å^3, 4615 reflections collected of which 2059 unique (R_{int} = 0.0329). R_1 = 0.0304 ($I > 2\sigma(I)$), wR_2 = 0.0851 (all data).

Crystal data for CaFRUI (M = 690.22 g/mol): monoclinic, space group C2, Z = 2, a = 18.0605(15), b = 7.7022(2) Å, c = 11.3126(10) Å, β = 135.130(15)°, V = 1110.2(2) Å^3, 10,786 reflections collected of which 5330 unique (R_{int} = 0.0311). R_1 = 0.0350 ($I > 2\sigma(I)$), wR_2 = 0.0691 (all data).

All atoms but hydrogens were refined with anisotropic thermal factors. Even if the hydrogen's peaks were observed in the difference Fourier maps, hydrogen atoms were calculated and refined riding with the U_{iso} = 1.2 or 1.5 U_{eq} of the connected atom. The interested reader can find further details on crystal data, data collection, least-squares refinements, and bond lengths in the Supporting Information (Tables S1−S3) and CIF files (CCDC 2170706-2170707-2170708).

Computational Methods. *Nanoparticle Calculations.* Calculations were performed with the GAUSSIAN16 set of programs.[12] All the structures in this work were optimized using gradient-based techniques[13−16] with no symmetry constraints at the DFT B3LYP level of theory,[17,18] in conjunction with the 6-31G(d) basis set for the C, H, O, Ca, and Br atoms.[19] For Sr and I, the LANL2DZ basis was used.[20] The geometry of the SrRIBBr complex was also optimized with the aug-cc-pVDZ basis set; for Sr, the basis used was aug-cc-pVDZ-PP with the ECP28MDF Stuttgart/Koeln pseudopotentials.[21,22]

All critical points were characterized as energy minima by calculating the analytical frequencies. The total dipole moment, polarizability, and the first-order hyperpolarizability were calculated at the same level of theory. Ab initio volume calculations based on numerical Monte Carlo integration introduce a large degree of error. To compute the molar volume in a more quantitative way, tight convergence in the self-consistent field procedure and increased density of points for more accurate integration were employed. Molecular volumes were computed by averaging 10 different volume calculations on the optimized geometries at the B3LYP level of theory with the options scf = tight, volume = tight, and iop(6/45 = 500, 6/46 = 1).[23]

Bulk Calculations. In-crystal DFT PBE0 periodic quantum simulations were performed with the linear combination of the Gaussian-type function (LCGTF) approach as implemented in the CRYSTAL17 package.[24,25] The same computational procedure described in detail elsewhere[26,27] was applied. For each crystal structure, the atomic coordinates were fully relaxed at fixed experimental unit cell parameters under crystallographic symmetry constraints. CaRIBr and SrRIBBr compounds are conformationally disordered. For these structures, both the occupied sites in the unit cell were considered as starting points, leading to two symmetry-independent sets of relaxed atomic coordinates. All the optimized geometries underwent coupled-perturbed (CP) Kohn−Sham simulations to estimate the first-order and second-order polarizabilities.[28−30] For the disordered structures, the final NLO outcomes were averaged over both the structural models, using experimental site occupation factors (sofs) as weights. Basis set coefficients, as well as the optimized coordinates of each asymmetric unit, are deposited in Section S1 of the Supporting Information.

SHG Measurements. The SHG efficiency of the powdered compounds was measured using the Kurtz and Perry method.[31] Samples were ground in an agate mortar (grain sizes below 100 μm) and heated in a stove at 323 K to avoid the absorption of humidity before being sealed into capillaries.

The nonresonant 1064 nm wavelength of a Nd:YAG pulsed laser beam was directed on capillaries containing the samples. The scattered radiation was collected using an elliptical mirror, filtered to select only the second-order contribution at 532 nm (I^{2w}), and recollected with a Hamamatsu R 5108 photomultiplier tube. The SHG efficiency was evaluated by taking as reference the SHG signal of ground sucrose powder ($I^{2w}/I^{2w}_{sucrose}$).

■ RESULTS AND DISCUSSION

Crystal Structure Description of CaRIBBr and SrRIBBr. D-ribose is a natural aldo-pentose sugar that is a component of the ribonucleotides from which the nucleic acid RNA is built. In aqueous solution at room temperature, the pyranose is the dominant form, while the mutarotation equilibrium is shifted toward the β anomer roughly in a 2:1 ratio (β: 58.5%; α: 21.5%).[32] As other simple sugars, exhibiting many OH groups that interact easily with metals, D-ribose shows the ability to bind many metal ions,[33] especially alkali-earth and post-transition metals. Despite the importance to understand the physiological behavior of the interaction between calcium and

https://doi.org/10.1021/acs.cgd.2c00560
Cryst. Growth Des. 2022, 22, 5923−5934

strontium with D-ribose, until now, the X-ray crystal structures of Ca- or Sr-ribose complexes were not determined.

The two compounds are almost perfectly isostructural, with a slightly larger (+2.2%) cell volume of the Sr-containing crystal that does not imply any significant change in the packing motifs. Thus, any difference in the optical behavior of the two compounds is expected to be due to the different chemical nature of the cation.

The asymmetric unit of both compounds (Figure 1) consists of half M^{2+} ion, one Br^- anion, one ribose molecule with three OH groups (O2, O3, and O4) connected to the calcium ion, and one water molecule (O1W) and a half (O2W) both coordinated to the metal atom. The whole molecule is obtained applying the twofold axis through the M−O2W bond and is composed of two ribose three-chelating molecules and three water molecules coordinated to the M^{2+} (Figure 2). The bromine ions are connected to two OH groups of the sugar with strong hydrogen bonds (O2−H2···Br1 = 2.45/2.46 Å, O4−H4···Br1 = 2.45/2.48 Å for Ca/SrRIBBr, respectively).

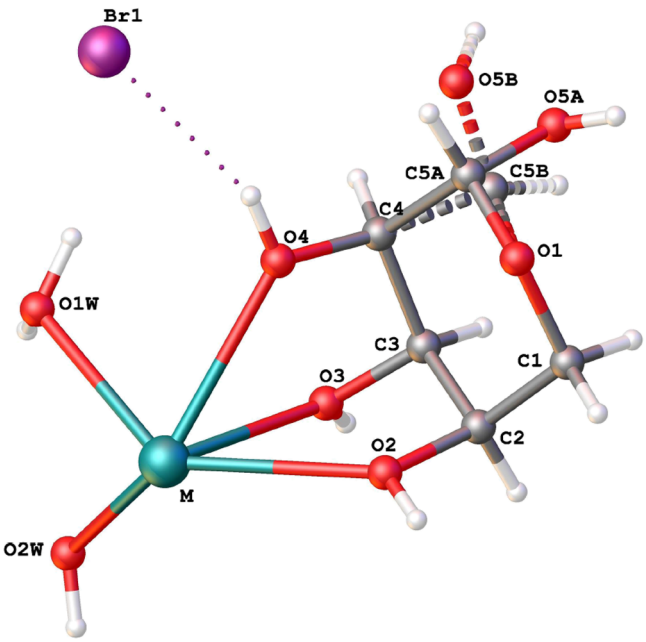

Figure 1. View of the asymmetric unit of the compounds MRIBBr (M = Ca, Sr).

The ribose molecule adopts the D-ribopyranoside form, both in the α and β-configuration (see Scheme 1) because the O(5)-H(5) is disordered into two positions: the α/β relative site occupation factors are 50/50% in CaRIBBr and 23/77% in SrRIBBr, as determined by least-squares refinements against measured structure factor amplitudes. It could be tempting to suggest that Ca^{2+} ions might favor the crystallization of the α−D−ribopyranose form with respect to the anomeric equilibrium in solution,[32] but it is hard to say whether this is a genuine chemical effect or it can be ascribed to fine details of the crystallization conditions. Studies focused on specific crystallization aspects are needed to gain insights into the matter.

Contrary to the similar compounds considered in our previous studies, in these two structures, ribose molecules do not form infinite chains or planes of metal-sugar fragments typical of MOF structures, but the structures are simply molecular crystals. The $[M(ribose)_2(H_2O)_3]^{2+}$ molecules are aligned along the b axis (Figure 2) and are connected through strong hydrogen bonds that involve the oxygen of the pyranose ring (O1) and two symmetrical equivalent hydroxyl groups of the following molecule (O3−H3···O1 = 2.07/1.96 Å for Ca/SrRIBBr, respectively).

These rows of molecules are connected to each other through strong hydrogen bonds that involve the OH groups of the ribose, the water molecules, and the Br^- ions (Table S2 of the Supporting Information).

Crystal Structure Description of CaFRUI. The asymmetric unit of CaFRUI (Figure 3) consists of half Ca^{2+} ion, one I^- anion, one fructose molecule with two OH groups (O2 and O3) connected to the calcium ion, and one water molecule (O1W) coordinated to the metal atom. The D-fructose ligand in CaFRUI is present in the six-membered β−D−fructopyranoside cyclic form.

Applying the twofold axis passing through the metal atom and the translation along the *b* axis, an infinite chain is formed where each metal cation is surrounded by four sugar and two water molecules (Figure 4). The iodide ions are connected to three OH groups of the sugars with strong hydrogen bonds (O2−H2···I1 = 2.630 Å, O4−H4···I1 = 2.602 Å, and O1W−H1WA···I1 = 2.882 Å). The chains are connected to each other through strong hydrogen bonds that involve the OH groups of the fructose and the water molecules and the I^- ions (Table S3 of the Supporting Information).

The CaFRUI structure is a 1D MOF and is very similar to the structures of MFRUX compounds (M = Ca, Sr; X = Cl, Br) studied in the past by our group,[34] except for the absence of the crystallization water molecules between the chains.

Computational Results. The theoretical calculations were performed with two methods, one working on nanoparticle sizes and one considering the infinite crystal (bulk calculations), the two extreme situations between which the "real" powder dimensions should lie.

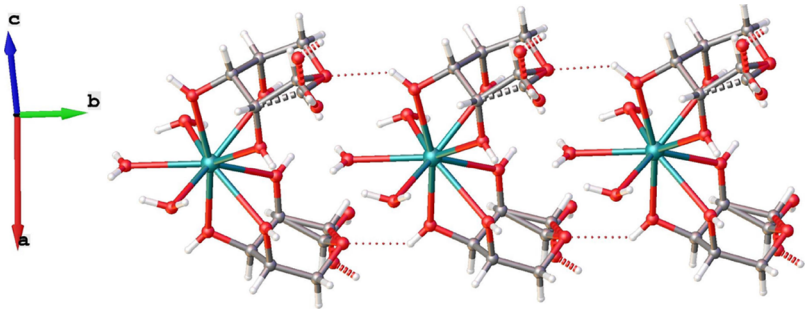

Figure 2. View of the packing motif along the [0 1 0] direction.

https://doi.org/10.1021/acs.cgd.2c00560
Cryst. Growth Des. 2022, 22, 5923−5934

Scheme 1. Isomer and Anomer Forms of D-Ribose in Aqueous Solution

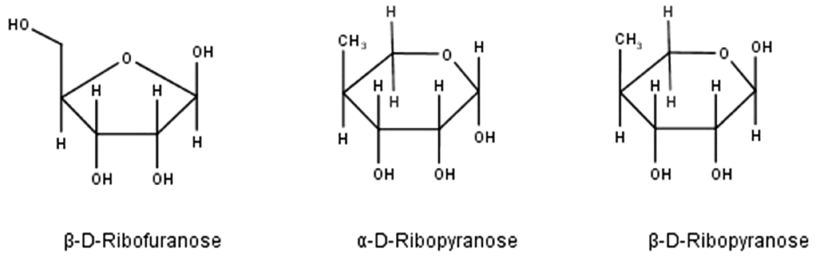

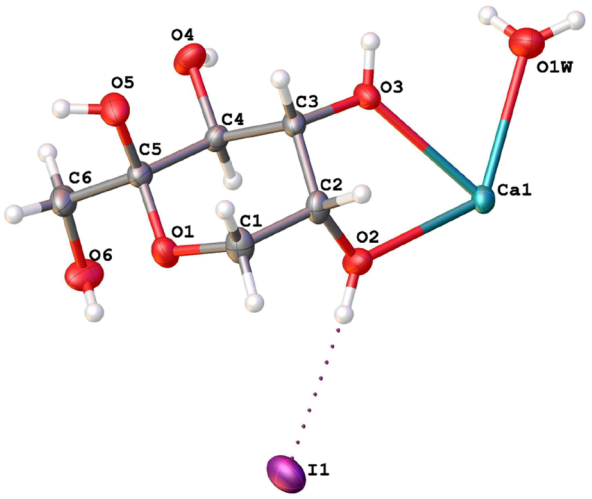

Figure 3. View of the asymmetric unit of CaFRUI.

Nanoparticle Calculations. Theoretical calculations were performed taking into account that the experimental SHG measurements are carried out on crystalline powders of micro- or submicro size. To better simulate the size of the particles, small fragments of the same size but with different shapes were selected starting from the X-ray structures. These models allow to take into account the structural distortion that the surface forces can induce at the nanoscale level.

In Figure 5 is reported the Frag_1 of MRIBBr complexes selected by cutting the crystal along the one-dimensional M-ribose chain and is composed of three M = (Ca, Sr) ions, six ribose molecules, six Br anions, and nine water molecule, while in Figure 6, the Frag_2 of the same complexes is obtained by cutting the crystal along two parallel M-ribose chains connected through several hydrogen bonds and with the same chemical composition of the Frag_1.

The geometrical optimized parameters reported in Table 1 generally show small deviations from the corresponding X-ray data; in some cases, larger deviations are observed probably due to the small size of the computed fragments, which involve a certain degree of asymmetry with respect to the crystal. The

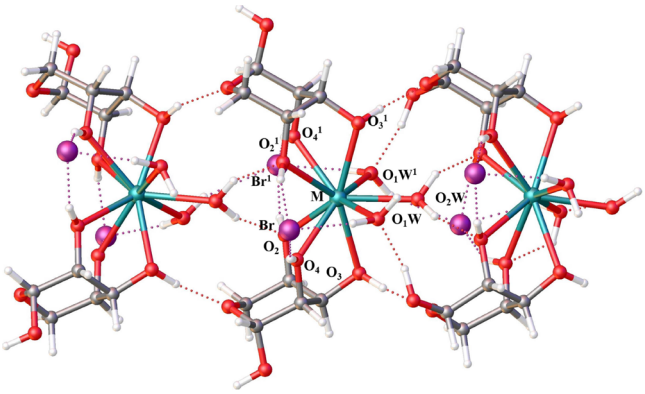

Figure 5. Frag_1 of the MRIBBr (M = Ca, Sr) compounds.

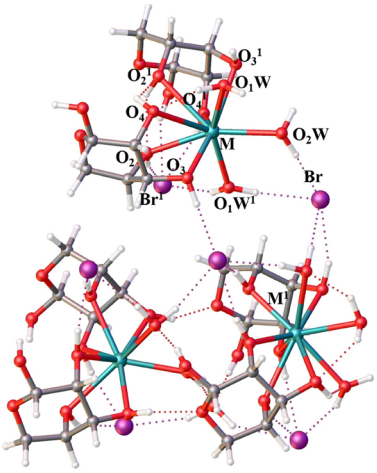

Figure 6. Frag_2 of the MRIBBr (M = Ca, Sr) compounds.

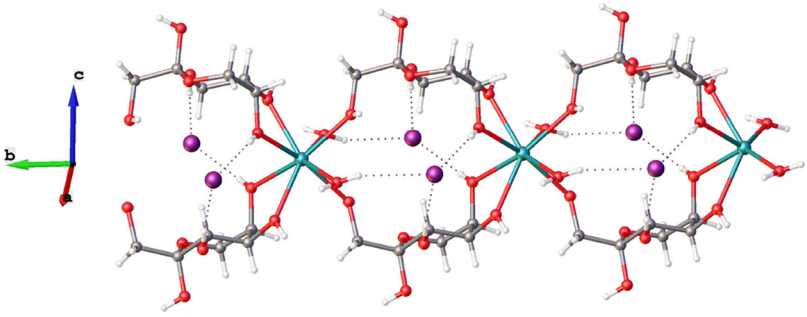

Figure 4. View of the packing motif CaFRUI along the [0 1 0] direction.

https://doi.org/10.1021/acs.cgd.2c00560
Cryst. Growth Des. 2022, 22, 5923−5934

Table 1. Relevant Distances (Å) from X-ray Data and from Computational Calculations of Frag_1 and Frag_2 of MRIBBr Compounds (M = Ca, Sr)[a]

M = Ca, Sr	CaRIBBr			SrRIBBr			
	XRD	Frag_1	Frag_2	XRD	Frag_1	Frag_1a[b]	Frag_2
M−O1W	2.522(7)	2.616	2.478	2.623(5)	2.652	2.724	2.689
M−O2W	2.47(1)	2.556	2.581	2.577(8)	2.582	2.595	2.703
M−O2	2.519(6)	2.541	2.577	2.636(4)	2.628	2.616	2.728
M−O3	2.391(5)	2.555	2.509	2.588(5)	2.733	2.694	2.671
M−O4	2.576(5)	2.532	2.537	2.656(4)	2.675	2.673	2.622
C1−O1	1.44(1)	1.428	1.420	1.446(9)	1.428	1.432	1.420
C5A−O1C5B−O1	1.44(2)1.39(2)	1.424	1.431	1.40(1)1.39(2)	1.423	1.424	1.433
C2−O2	1.426(8)	1.424	1.430	1.453(7)	1.420	1.425	1.430
C3−O3	1.43(1)	1.430	1.431	1.441(9)	1.431	1.434	1.430
C4−O4	1.412(8)	1.422	1.425	1.438(7)	1.420	1.423	1.427
C1−C2	1.49(1)	1.532	1.528	1.49(1)	1.533	1.537	1.529
C2−C3	1.51(1)	1.538	1.536	1.50(1)	1.539	1.536	1.539
C3−C4	1.50(1)	1.536	1.536	1.50(1)	1.538	1.536	1.544
C4−C5AC4−C5B	1.53(2)1.59(2)	1.498	1.550	1.55(1)1.55(2)	1.543	1.543	1.550
C5A−O5AC5B−O5B	1.33(2)1.46(2)	1.396	1.377	1.41(1)1.37(4)	1.396	1.403	1.376
M···M[c]	6.567	6.077	6.340	6.771	6.287	6.398	5.319
M···M[d]	9.303	//	7.858	9.305	//	//	7.214
M···Br av.	4.848	4.408	4.049	4.927	4.499	4.475	4.200
Br···Br[c]av.	8.232	8.095	7.333	8.222	8.194	8.258	7.602

[a]All theoretical distances are averaged for the chemically equivalent bonds of the fragments. [b]Calculated at the B3LYP/aug-cc-pVDZ level of theory. [c]Distance between metals of the same chain. [d]Distance between metals of adjacent chains.

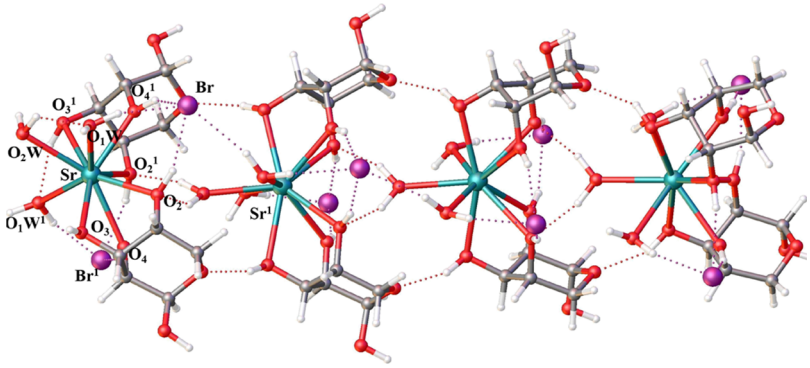

Figure 7. Frag_3 of the SrRIBBr.

most relevant differences between the X-ray data and the theoretical calculations are found in the bonds between the metal and the coordinated oxygen atoms and range from a minimum of 0.005 Å of Sr−O2W to a maximum of 0.16 Å of Ca−O3 in Frag_1.

Greater differences are observed in the distances M···M, M···Br, and Br···Br that range from a minimum of 0.1 Å for the Br···Br distance in Frag_1 of CaRIBBR to 2.0 Å in M···M[c] distance of SrRIBBr in Frag_2. However, it should be pointed out that in the small fragments considered for the theoretical calculations, not all the M···Br and Br···Br bonds expected from the X-ray structure are present. The differences between the results of experimental measures and theoretical calculation are probably also caused by the difficulty that DFT with double-ζ basis sets has to describe the noncovalently bound moieties; in fact, these differences indicate a shorter distance between the sugar molecules in the theoretical model.

Table 1 also shows the geometrical parameters of Frag_1a optimized at the B3LYP level but with the aug-cc-pVDZ bases set. The geometry of Frag_1a does not show significant differences from Frag_1. In Figure 7 is reported the Frag_3 of SrRIBBr complex selected by cutting the crystal along the one-dimensional Sr-ribose chain, composed of 4 Sr ions, eight ribose molecules, eight Br anions, and 12 water molecules. As shown in Figure 8, the Frag_4 of the same complexes is obtained by cutting the crystal along two parallel Sr-ribose chains, connected through several hydrogen bonds and with the same chemical composition of the Frag_3. As shown in Figure 9, Frag_5 consists on a chain of 5 Sr ions, 10 Ribose molecules, 10 Br anions, and 15 water molecules.

Table 2 shows the most important optimized parameters related to Frag_3, Frag_4, and Frag_5, together with the results of the corresponding X-ray data. Small deviations are observed for the C−O and C−C bonds in all fragments with respect to the corresponding X-ray data. The largest deviations occur in the bonds between the metal and the coordinated oxygen atoms and range from a minimum of 0.08 Å for Sr−O1W in Frag_3 to a maximum of 0.18 Å for Sr−O3 in Frag_4 and Frag_5. Greater differences are observed in the distances Sr···Sr, Sr···Br, and Br···Br, for which a maximum of 0.6 Å for the Sr···Sr distance in Frag_5 is observed.

https://doi.org/10.1021/acs.cgd.2c00560
Cryst. Growth Des. 2022, 22, 5923−5934

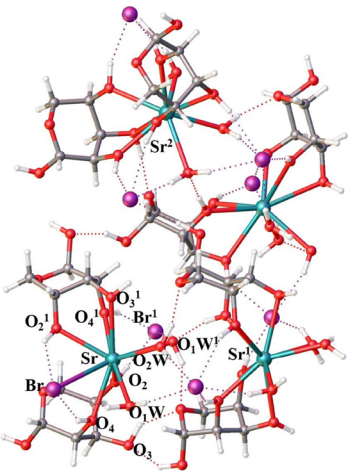

Figure 8. Frag_4 of the SrRIBBr.

In Figures 10 and 11 are reported the fragments selected from the X-ray structure of CaFRUI. Frag_1 is obtained by cutting the crystal along the one-dimensional Ca-fructose chain and is composed of three Ca^{2+} ions, six fructose molecules, six Br^- anions, and six water molecules. Frag_2 consists of three Ca^{2+} ions, eight fructose molecules, six Br anions, and six water molecules selected by cutting the crystal along two adjacent chains.

Table 3 shows the most relevant geometrical parameters optimized for CaFRUI compared with the corresponding X-ray data. Also, in this complex, the most relevant differences between the X-ray data and the theoretical calculations are found in the bonds between the metal and the coordinated oxygens and range from a minimum of 0.002 Å of Ca1−O3[b] in Frag_2 to a maximum of 0.14 Å of Ca1−O6[d] in Frag_1. Greater differences are observed, also in the CaFRUI complex, in the distances Ca···Ca, Ca···I and I···I: these distances are generally shorter than the ones of the X-ray and reflect the effects of surface forces on the nanoparticles.

The density functional theory (DFT/B3LYP) with the 6-31G(d) basis was also used to calculate the dipole moment μ, mean polarizability $<\alpha>$, and first static hyperpolarizability β. Because the aim of the work is to compare the trend of these properties in complexes based on different sugars and salts, the values of dipole moment, polarizability, and hyperpolarizability calculated at the same level of theory and with the same basis set for the molecules considered can provide a satisfactory comparison of these quantities. To verify the effect of the diffuse functions on the hyperpolarizability calculation, we also optimized the SrRIBBr complex using the aug-cc-pVDZ basis.

Table 2. Relevant Distances (Å) from X-ray Data and from Computational Calculations of SrRIBBr Fragments[a]

	SrRIBBr			
bond	XRD	Frag 3	Frag 4	Frag 5
Sr−O1W	2.623(5)	2.707	2.745	2.697
Sr−O2W	2.577(8)	2.578	2.634	2.606
Sr−O2	2.636(4)	2.653	2.661	2.647
Sr−O3	2.588(5)	2.705	2.766	2.763
Sr−O4	2.656(4)	2.665	2.618	2.696
C1−O1	1.446(9)	1.434	1.429	1.433
C5A−O1	1.40(1)	1.417	1.419	1.421
C5B−O1	1.39(2)	//	//	//
C2−O2	1.453(7)	1.423	1.428	1.419
C3−O3	1.441(9)	1.430	1.430	1.426
C4−O4	1.438(7)	1.416	1.418	1.422
C1−C2	1.486(1)	1.533	1.534	1.532
C2−C3	1.504(1)	1.540	1.543	1.541
C3−C4	1.505(1)	1.535	1.538	1.538
C4−C5A	1.55(1)	1.541	1.539	1.540
C4−C5B	1.55(2)	//	//	//
C5A−O5A	1.41(1)	1.410	1.418	1.421
C5B−O5B	1.37(4)	//	//	//
Sr−Sr[b]	6.771	6.307	6.231	6.138
Sr−Sr[c]	9.303	//	9.442	//
Sr−Br av.	4.927	4.518	4.387	4.452
Br−Br[b] av.	8.222	8.218	8.472	8.013

[a]All theoretical distances are averaged for the chemically equivalent bonds of the fragments. [b]Distance between metals of the same chain. [c]Distance between metal of adjacent chains.

In Table 4 are reported the computed values of the dipole moment μ, the mean polarizability α, and an estimate of the intrinsic molecular hyperpolarizability (β) in the absence of any resonance effect, represented by a third rank tensor. The 27 components of the 3D matrix can be reduced to 10 components according to Kleinman symmetry. The Gaussian16 output file provides the main 10 components (β_{xxx}, β_{xxy}, β_{xyy}, β_{yyy}, β_{xxz}, β_{xyz}, β_{yyz}, β_{xzz}, β_{yzz}, and β_{zzz}), whose values for the studied compounds are given in Tables S10−S15. The magnitude of the total first hyperpolarizability (β_{tot}) can be defined as

$$\beta_{tot} = \sqrt{(\beta_{xxx} + \beta_{xyy} + \beta_{xzz})^2 + (\beta_{xxy} + \beta_{yyy} + \beta_{yzz})^2 + (\beta_{xxz} + \beta_{zyy} + \beta_{zzz})^2} \quad (1)$$

The relationship between the macroscopic second-order susceptibility, the quantity correlated to the second harmonic

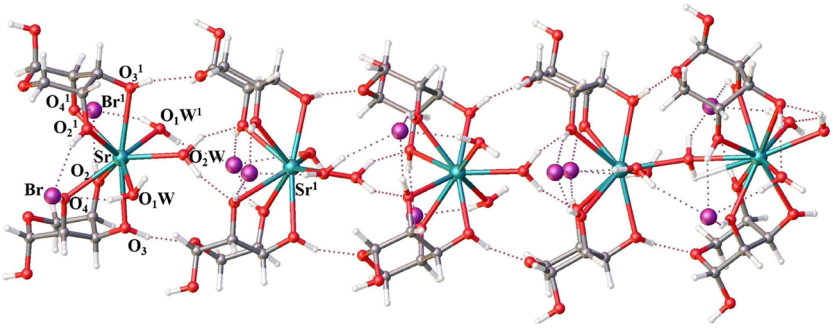

Figure 9. Frag_5 of the SrRIBBr.

https://doi.org/10.1021/acs.cgd.2c00560
Cryst. Growth Des. 2022, 22, 5923−5934

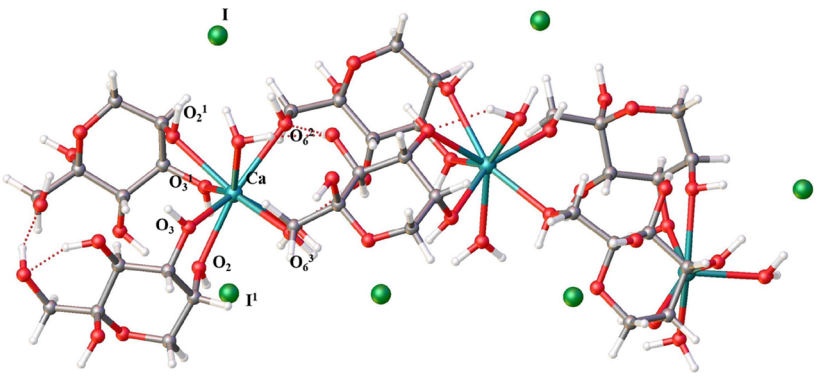

Figure 10. Frag_1 of the CaFRUI compound.

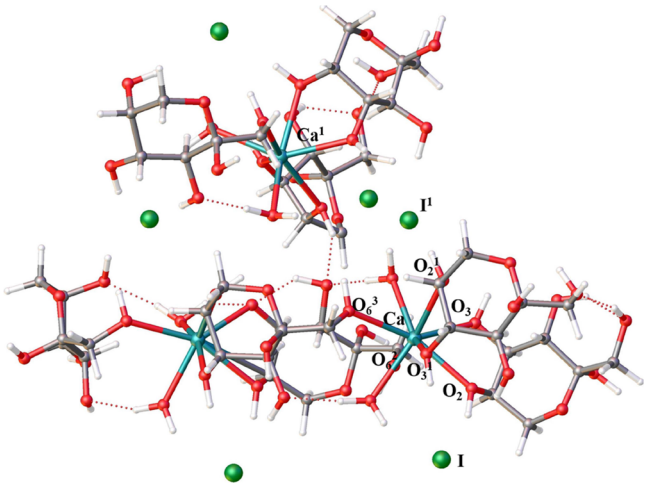

Figure 11. Frag_2 of the CaFRUI compound.

intensity, and the microscopic hyperpolarizability is given by eq 2[35]

$$\chi^{(2)} = \beta_{tot} \cdot NF \quad (2)$$

where N is the number of particles per unit volume and F is the local field factor. F depends on the crystal symmetry, and it is related to the refractive index of the crystal. Values between 1 and 2 are generally reported, and in particular, for saccharides, this value ranges between 1.5−1.6.[34] We assume $F = 1$ because our interest is focused on the trend of the ratio $\chi^{(2)}/\chi^{(2)}_{sucrose}$. The ratios between the second-order susceptibility of the compounds and that of sucrose are also reported in Table 3.

A first point that deserves attention is the influence of the basis set. While the optimized geometries do not depend on the level of theory adopted (Table 1), significant changes affect polarizability and second-order response parameters when an extended aug-cc-pVDZ basis set is employed (compare columns "Frag_1" and "Frag_1a" for the SrRIBBr structure). However, both hyperpolarizability and second-order susceptivities are invariably reduced by the extended basis set, implying that 6-31G(d) results provide maximum estimates; real values are probably smaller. However, comparison of 6-31G(d) predictions on nanoparticles throughout the sugar-based MOF series, although clearly approximate *per se*, can provide reliable hints on a relative scale for the expected NLO performances. This is confirmed by the substantial agreement with trends obtained from periodic quantum simulations and NLO experiments, certified also by the statistical multivariate analysis (see *infra*). From Table 4, we observe that for the two ribose complexes, the values of the total intrinsic hyperpolarizability are very different for the fragments, that is, for the SrRIBBr, the value of the β_{tot} of the fragments with a linear structure (Frag_1, Frag_3, Frag_5) is greater than the others. The β_{tot} values show that they do not depend on the size of the macromolecule, but rather on the nature and structure of the particles, because the greatest value is found in the smallest fragment. This trend is also observed in the dipole moments values, while the values of α is more dependent on the size of the fragment. The second-order susceptibility and

Table 3. Relevant Distances (Å) from X-ray Data and from Computational Calculations for Frag_1 and Frag_2 of CaFRUI[a]

	XRD	Frag_1	Frag_2
Ca1−O1W	2.546(3)	2.507	2.461
Ca1−O1W[b]	2.546(3)	2.472	2.474
Ca1−O2	2.425(2)	2.555	2.547
Ca1−O2[b]	2.425(2)	2.550	2.511
Ca1−O3	2.466(2)	2.545	2.476
Ca1−O3[b]	2.466(2)	2.498	2.468
Ca1−O6[c]	2.423(2)	2.520	//
Ca1−O6[d]	2.423(2)	2.562	2.507
Ca1−O6[e]	2.423(2)	//	2.479
O1−C1	1.435(4)	1.427	1.434
O1−C5	1.412(4)	1.429	1.422
O2−C2	1.437(4)	1.439	1.436
O3−C3	1.435(4)	1.434	1.428
O4−C4	1.430(3)	1.417	1.421
O5−C5	1.412(4)	1.407	1.422
O6−C6	1.430(4)	1.425	1.434
C1−C2	1.507(5)	1.528	1.527
C2−C3	1.511(5)	1.530	1.538
C3−C4	1.517(5)	1.531	1.534
C4−C5	1.534(5)	1.543	1.541
C5−C6	1.520(4)	1.537	1.538
Ca···Ca[f]	7.702	7.364	7.466
Ca···Ca[g]	8.919	//	6.577
Ca···I av.	5.311	4.405	4.686
I···I av.	7.702	//	8.014

[a]All theoretical distances are averaged for the chemically equivalent bonds of the fragments. All theoretical distances are averaged for the chemically equivalent bonds of the fragments. [b]−1 − X,+Y,−2 − Z. [c] +X,−1 + Y,+Z. [d]−1 − X,−1 + Y,−2 − Z. [e]+X,1 + Y,+Z. [f]Distance between metals of the same chain. [g]Distance between metals of adjacent chains.

https://doi.org/10.1021/acs.cgd.2c00560
Cryst. Growth Des. 2022, 22, 5923−5934

Table 4. Computed Dipole Moments μ (Debye), Mean Polarizabilities α (a.u.), First Static Hyperpolarizabilities β_{tot} (10^{-30} cm^5 esu^{-1}), Second-Order Susceptibilities $\chi^{(2)}$ (pm V^{-1}), and Second-Order Susceptibilities Ratios with Respect to Sucrose Values

	CaRIBBr			SrRIBBr					CaFRUI	
	Frag_1	Frag_2	Frag_1	Frag_1a[a]	Frag_2	Frag_3	Frag_4	Frag_5	Frag_1	Frag_2
μ	40.0	18.6	42.3	41.0	19.2	55.3	18.2	75.5	11.5	9.8
α	657.0	664.5	644.2	821.7	650.7	859.8	866.2	1080.1	744.9	914.1
β_{tot}	15.5	11.1	20.1	8.7	12.0	18.1	15.0	19.0	15.4	14.7
$\chi^{(2)}$	3.3	2.4	4.1	1.8	2.5	2.8	2.4	2.4	2.0	2.2
$\chi^{(2)}/\chi^{(2)}_{sucrose}$	2.3	1.7	2.9	1.3	1.8	2.0	1.7	1.7	1.4	1.6

[a]Calculated at the B3LYP/aug-cc-pVDZ.

the ratio between the susceptibilities maintain this trend, although reduced by the dependence on the molar volumes.[35,36] For the CaFRUI complex, all the properties calculated are much more similar in both fragments. These results, together with those of the previous work,[37] indicate that the geometry of the selected fragments in some cases greatly affect the calculated properties. The hyperpolarizability and second-order susceptibility of the Frag_1a calculated at the B3LYP/aug-cc-pVDZ level of theory are much lower than the other values, despite the fact that the dipole moment and polarizability are very similar. Unfortunately, a single result is not enough to reach any conclusions.

Bulk Computational Results. As reported above, the MRIBBr compounds show α and β-configuration disorders. We dealt with this disorder by applying the same strategy employed in our previous studies.[38] The X-ray structure was split into two fully ordered models, differing in the relative orientation of the anomeric substituents. Atomic positions were optimized independently and self-consistently in the crystal by solving the Schrödinger equation. The corresponding Bloch-compliant wavefunctions underwent independent CP simulations under an external electric field. The predicted optical properties were averaged over the two structures, using the experimental site occupation factors as relative weights.

The root mean square displacement (RMSD) estimates between the X-ray structures and the DFT-optimized structures are all below 0.1 Å (Figure S1 of the Supporting Information), the largest deviations concerning, as expected, the orientation of terminal hydrogen atoms. We thus conclude that our quantum models correctly reproduce the experimental geometries, as well as the packing and coordination features, of the title compounds. Quantum simulations predict static dielectric susceptivities for these ideal crystal structures at 0 K: no contributions besides the electronic ones are included, in the limit of very high electromagnetic frequencies. Because of the intrinsic nonideality of the experiments, any comparison among measured and predicted NLO properties always comes with many if and buts. However, all the NLO measurements were carried out on micrometer-sized grains, and it is reasonable to hypothesize that the coherence length is lower than average crystallite dimensions. Under these conditions, the second harmonic efficiencies should not depend on the particle size,[26,27] and we can assume that the second-order intensity is proportional to the square averaged $\langle(ijk)^2\rangle$ second-order polarizability tensor elements. Thus, it is possible to evaluate the relative expected NLO response with respect to pure sucrose, taken as a suitable standard reference. The results for the title materials are summarized in Table 5, while Table 6 shows the corresponding predicted first- and second-order optical responses.

Table 5. Ratio between the Average Second-Order Squared Susceptibility Tensor Elements With Respect to Crystalline Sucrose As Estimated through Bulk Calculations

	CaRIBBr	SrRIBBr	CaFRUI
$<d_{ijk}^2>/<d_{ijk}^2>_{sucrose}$ (*bulk*)	3.4	4.4	9.6

Table 6. DFT−Derived First-Order Electric Susceptivities ($\chi^{(1)}$, Dimensionless), Diagonalized Dielectric Tensor Elements (ε, Dimensionless)[a] and Second-Order Electric Susceptivities ($\chi^{(2)}$, Atomic Units)[b] for CaRIBBr, SRRIBr and CaFRUI (All in Space Group *C*2)

substance	CaRIBBr		SrRIBBr		CaFRUI
anomer	β	α	β	α	no disorder
sof[c]	50	50	72.4	27.6	100
$\chi_{xx}^{(1)}$	1.1709	1.1637	1.0844	1.0951	1.1905
$\chi_{xz}^{(1)}$	−0.0306	−0.044	0.0232	0.0151	0.0403
$\chi_{yy}^{(1)}$	1.1643	1.1592	1.0902	1.0923	1.2212
$\chi_{zz}^{(1)}$	1.2286	1.2037	1.1306	1.1611	1.2269
ε_{11}	2.1577	2.1353	2.0747	2.0919	2.1644
ε_{22}	2.1643	2.1592	2.0902	2.0923	2.2212
ε_{33}	2.2418	2.2321	2.1402	2.1644	2.2529
$\chi_{xxy}^{(2)}$	0.0446	0.1947	−0.0518	0.0273	−0.3531
$\chi_{xyz}^{(2)}$	−0.1287	0.0277	−0.0787	−0.2080	0.2254
$\chi_{yyy}^{(2)}$	0.4877	0.1062	−0.4115	−0.6389	−0.1157
$\chi_{yzz}^{(2)}$	−0.4733	−0.4900	0.5429	0.4950	0.7972

[a]Diagonal elements of the dielectric tensor, ε, in the principal axes system. [b]Second-order susceptivities can be expressed in other conventions through the usual conversion factors. Frequent alternative expressions of the second-order tensor components as β_{ijk} or d_{ijk} quantities (always in atomic units) are $\beta_{ijk} = (V\cdot\chi_{ijk})/2\pi$, V being the unit cell volume in cubic bohr, and $d_{ijk} = \chi_{ijk}/2$. Conversion to the MKS system in terms of reciprocal electric field units can be accomplished according to d_{ijk}(MKS) = d_{ijk}(a.u.)/0.514220632 pm/V. See also www.physics.nist.gov/constants. [c]Site occupation factor (%). In Sr-containing MOFs, both anomers are present in the same crystal, which is a disordered solution.

The average NLO response of the two isostructural ribose-containing compounds is very similar, and thus, in this case, the change of the cation should have no detectable effect on the optical response (Tables 5 and 6). On the basis of bulk simulations, the fructose compound CaFRUI is predicted to perform almost 3 times better than CaRIBBr (Table 5), which contains the same cation. However, it is difficult to disentangle the effect of the sugar − and the consequent slightly different coordination geometry − from contributions due to the highly polarizable iodine anion. The disorder at the anomeric carbon atoms further complicate the picture.

https://doi.org/10.1021/acs.cgd.2c00560
Cryst. Growth Des. 2022, 22, 5923−5934

Table 7. Ratio between the Average Second-Order Susceptibilities With Respect to the Sucrose Values Obtained from the Nanoparticle Calculations, the Ratio between the Average Second-Order Squared Susceptibility Tensor Elements With Respect to Crystalline Sucrose As Estimated through Bulk Calculations, the Ratio between the Second Harmonic Signal Produced by Powdered Samples and That of Standard Sucrose in the Same Experimental Conditions

	space group	nanoparticle$\chi^2/\chi^2_{sucrose}$	bulk$\langle d_{ijk}^2\rangle/\langle d_{ijk}^2\rangle_{sucrose}$	$I^{2w}/I^{2w}_{sucrose}$
CaFRUCl_a[27] [Ca(β-D-fructose)$(H_2O)_2$]Cl_2	$P2_1$	2.2	3.2	0.5
CaFRUCl[34] [Ca(β-D-fructose)$_2(H_2O)_2$]$Cl_2\cdot H_2O$	C2	2.0	1.4	0.3
CaFRUBr[34] [Ca(β-D-fructose)$_2(H_2O)_2$]$Br_2\cdot H_2O$	C2	2.5	3.3	0.2
CaFRUI[a] [Ca$(C_6H_{12}O_6)_2(H_2O)_2$]I_2	C2	1.5	9.6	0.1
SrFRUCl[34] [Sr(β-D-fructose)$_2(H_2O)_2$]$Cl_2\cdot H_2O$	C2	2.1	0.5	0.2
SrFRUBr[34] [Sr(β-D-fructose)$_2(H_2O)_2$]$Br_2\cdot H_2O$	C2	2.4	2.9	0.6
SrFRUI[38] [Sr(β-D-fructose)$_2$]I_2	$P2_1$	3.0	19.2	10
SrFRUI4[38] [Sr_2(β-D-fructose)$_3(H_2O)_3$]$I_4\cdot 0.5H_2O$	$P2_12_12_1$	2.0		2.0
SrFRUI6[38] [Sr(β-D-fructose)$(H_2O)_3$I]I	$P2_12_12_1$	1.6	1.2	1.5
CaDGalBr[37] [Ca(2-deoxy-D-galactose)$_2$]Br_2	$P2_1$	1.0	1.50	0.6
CaDGalI[37] [Ca(2-deoxy-D-galactose)$_2$]I_2	$P2_1$	1.6	5.60	0.8
CaRIBBr[a] [Ca$(C_5H_{10}O_5)_2$]Br_2	C2	2.0	3.4	0.5
SrRIBBr[a] [Sr$(C_5H_{10}O_5)_2$]Br_2	C2	2.4	4.4	1.2

[a]The $\chi^2/\chi^2_{sucrose}$ ratios reported in this table are an average of those reported in Table 3.

SHG Measurements and Comparison with the Theoretical Calculations. To test the influence of the particles' size on the SHG response, we measured the SH intensities of one of the compounds, namely, SrFRUCl, for three different particle sizes obtained from different powder treatments: (i) not-ground crystals with a dimension of about 0.1 mm as revealed from the optical stereomicroscope; (ii) crystals hand-ground on an agate mortar with estimated dimension of c.a. 0.5−1 μm; (iii) crystals ground with a planetary ball mill for 66 min at 200 rpm with dimension ca. 135 nm as determined in one of our previous work.[39] The measured SH intensities ratio to sucrose were 0.4, 0.3, and 0.2. Undoubtedly, as expected, there is a lowering of the SH intensity ratio with the crystal dimension, but the differences are very low and the order of magnitude is preserved. Thus, to standardize the method, we decided to measure the SH intensities with the hand-ground powder for all the compounds discussed.

In Table 7, the experimental and theoretical SHG responses for the three compounds analyzed in this work are reported together with those of similar compounds previously studied by our group. For comparison purposes, the $I^{2w}/I^{2w}_{sucrose}$ experimental values of all compounds were measured with the Kurtz−Perry method, also in the case of the previously reported compounds, for which a different method was used. For the same reason, we predicted again the NLO responses also of the compounds CaFRUCl_a and MFRUX (M = Ca, Sr and X = Cl, Br) through DFT-CP solid-state simulations (Table S16 of Supporting Information).

The values of $\chi^2/\chi^2_{sucrose}$ for the nanoparticle calculations and of $\langle d_{ijk}^2\rangle/\langle d_{ijk}^2\rangle_{sucrose}$ for the bulk calculations cannot be directly compared but are both ratios to the sucrose response that can be correlated to the experimental $I^{2w}/I^{2w}_{sucrose}$. Thus, considering exclusively the trend of these values, we can assert that a qualitative agreement is observed among computational predictions and the experimental outcomes.

Multivariate Analysis of the SHG Behavior of Sugar-Metal Halide-Based Compounds. To see whether the NLO output can be correlated to relevant coordination and/or crystallographic features, we analyzed all the compounds in Table 6 through multivariate analysis. A principal component analysis (PCA) was performed to disentangle physical correlations from statistical noise. PCA is a powerful nonparametric tool to extract relevant information from redundant sets of crystallographic and electronic data.[40,41] The idea is to apply an orthogonal transformation in a suitably defined hyperspace of physical variables to define new variables, called principal components (PC), that correspond to the eigenvectors of the original variance−covariance matrix. The correlation coefficients between PC and original variables are called *loadings*. The latter define the weights of the linear combination of the initial variables to give the PCs. The coordinates of the original variables in the new reference frame are called *scores*. Inspection of scores and loadings in the PC frame can provide hints on the degree of cooperation of relevant variables in determining the observed physics. In the present case, the variables chosen to represent the system were (i) the coordination geometry (average metal-sugar oxygen distances), (ii) the crystal structure (cell volume, density), (iii) the metal and halogen scalar polarizabilities, α_0, and (iv) the NLO response relative to sucrose, as measured and predicted using quantum methods. A full list of variables can be found in the Supporting Information (Table S17). Figure 12 shows the PCA results.

The PCA analysis shows that the starting variables cluster into two distinct groups, which explain more than 70% of the sample variance. The first component (horizontal axis in Figure 12) is composed by structural parameters and atomic polarizabilities. This can be expected, as the cell density is related to average atomic weights, which correlate with polarizabilities, as heavier atoms bear more polarizable electrons. The second PC (vertical axis) describes instead the NLO response. It is worth noting that bulk DFT NLO predictions strongly correlate with the experimental results, and they both correlate with the nanoparticle estimates. This confirms the general accuracy of our computational approach.

More interesting is that the NLO response correlates only weakly with the structural variables. Accordingly, the scores are dispersed along the first principal axis, implying that the variables that describe the optical response are mostly ineffective to explain the variance of the data set. Thus, the nonlinear properties, which depend on the quantum excited states of the material, stem from a nonobvious interplay of structural, compositional, and electronic degrees of freedom,

https://doi.org/10.1021/acs.cgd.2c00560
Cryst. Growth Des. 2022, 22, 5923−5934

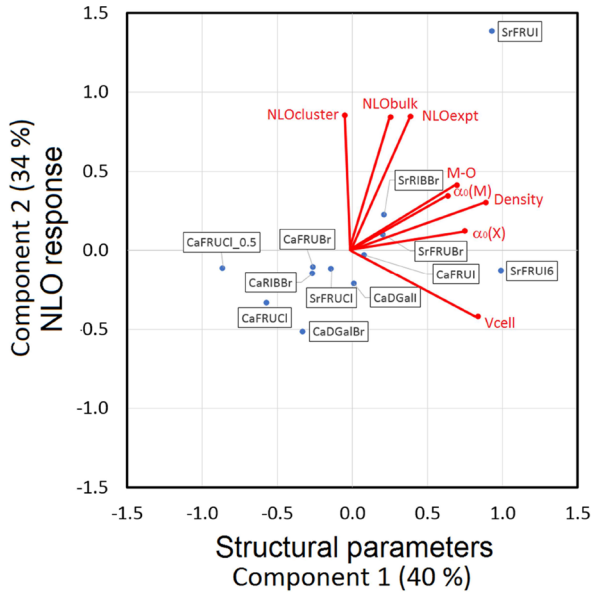

Figure 12. Biplot of the variable loadings (red lines) and scores (blue points) against the first (PC1, horizontal) and second (PC2, vertical) PC, with the percentage of variance explained. "NLO" axes mean the expected second-order relative intensity with respect to sucrose, as determined experimentally (expt) or by bulk and cluster simulations. α_0 are experimental atomic polarizabilities of the metal (M) and the halogen (X).[42] A common factor of 0.045 was applied to all the score moduli to bring them to a scale comparable with the plot dimensions. The varimax technique[43] was applied to rotate the PC frame so that the sum of the squared loadings is maximized in the new frame. The PCA analysis was performed through the aid of the Tanagra software.[44]

which cannot be rationalized in a simple model. Every now and then, some relationships can be recognized: for example, we note that iodine-containing materials have generally larger predicted NLO responses than isostructural Br-containing compounds. This is the case of the best-performing material SrFRUI, whose projection in the PC plane is dominated by its exceptional NLO output. However, CaFRUI (this work) shows only a weak experimental response, comparable to CaDGalI. To what extent this large variability is due to the cation (Ca^{2+} or Sr^{2+}), the sugar (fructose or deoxygalactose), or the crystal structure ($P2_1$ or $C2$) remains unclear.

Another interesting point is the role of general symmetry (that is, space group) in determining the overall NLO response. Only three space groups are represented in our data set, namely, C2, $P2_1$ and $P2_12_12_1$, with the orthorhombic symmetry occurring in just a minority of cases. A survey of Table 7 shows that $P2_12_12_1$ crystals are never associated with a strong NLO output, as expected based on the low number of active components in the hyperpolarizability tensor in the D_2 symmetry. On the other hand, both C2 and $P2_1$ space groups may sometimes convey a significant NLO response (SrFRUI, CaFRUI). Although patent correlations between the second harmonic output and the space group are hardly recognizable, we note that $P2_1$ crystals generally score better than C2 ones, but several exceptions exist.

Figure 13 shows box-and-whisker plots for the experimental and predicted NLO output vs space group. These summarize the sample spread and skewedness in the statistical population, with vertical bars ("whiskers") representing 1.5 times the interquartile range, that is, the distance between the upper and lower quartiles. The horizontal line within the box is the distribution mean. Outliers are displayed as individual data points. A take-home message is that $P2_1$ structures have a wider dispersion and access higher second harmonic responses than the C2 ones, but these performances are not systematic. For example, both experimental and bulk DFT estimates have distributions with similar mean values, which are placed in the lower half of the corresponding boxes. This implies that the NLO response is often low and comparable in $P2_1$ and C2 symmetries. The present statistics is necessarily partial, as it refers only to the three space groups in our sugar-based MOF data set. Safer conclusions may be reached by including more structures if they are accompanied by accurate NLO measurements. We defer a full statistical analysis of symmetries in luminescent MOFs to future studies.

■ CONCLUSIONS

This work aims to analyze what factors are responsible for the SHG behavior of metal halogenide-sugar-based compounds and reflects the difficulties to standardize the SHG predictions both for the theoretical calculation and mostly for the experimental measurements.

A possible take-home message, also in the context of our previous findings, is that DFT simulations can be considered at least as reliable predictors of the order of magnitude of the experimental results. Moreover, we propose that nanoparticle calculations not also represent a reasonable tradeoff between accuracy and computational requirements with respect to more demanding periodic simulations but they also take into account the finite size of the crystals in the powder and the lowering of symmetry because of their defects. This also implies that any strong NLO response must be originated by localized electronic states with a significant character of the metal, as well as by their interplay with those of the anion. As already noted,[37] the role of the crystal structure is to provide a

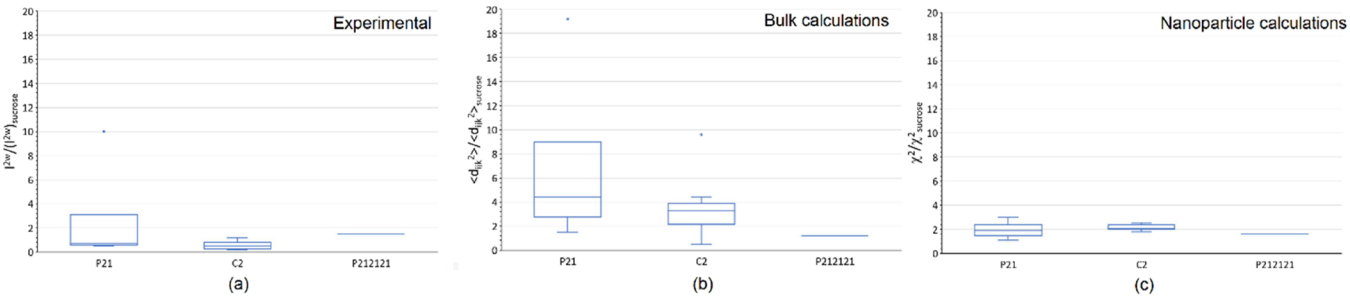

Figure 13. Box-and-whisker diagrams for the experimental (a) and predicted (b, c) NLO response.

https://doi.org/10.1021/acs.cgd.2c00560
Cryst. Growth Des. 2022, 22, 5923−5934

symmetry-breaking scaffold, ensuring that nonvanishing hyperpolarizability tensor elements are allowed.

■ ASSOCIATED CONTENT

Supporting Information

The Supporting Information is available free of charge at https://pubs.acs.org/doi/10.1021/acs.cgd.2c00560.

Details on crystal data and data collections and refinements, relevant bond distances, list of hydrogen bonds, details on theoretical calculations, and CIF files with structure factors embedded (PDF)

Accession Codes

CCDC 2170706−2170708 contain the supplementary crystallographic data for this paper. These data can be obtained free of charge via www.ccdc.cam.ac.uk/data_request/cif, or by emailing data_request@ccdc.cam.ac.uk, or by contacting The Cambridge Crystallographic Data Centre, 12 Union Road, Cambridge CB2 1EZ, UK; fax: +44 1223 336033.

■ AUTHOR INFORMATION

Corresponding Author

Domenica Marabello − *Department of Chemistry and CrisDi − Interdepartmental Center for Crystallography, University of Torino, Torino 10125, Italy;* orcid.org/0000-0002-9648-7735; Email: domenica.marabello@unito.it

Authors

Paola Antoniotti − *Department of Chemistry and CrisDi − Interdepartmental Center for Crystallography, University of Torino, Torino 10125, Italy;* orcid.org/0000-0003-2647-141X

Paola Benzi − *Department of Chemistry and CrisDi − Interdepartmental Center for Crystallography, University of Torino, Torino 10125, Italy;* orcid.org/0000-0001-7046-2022

Carlo Canepa − *Department of Chemistry, University of Torino, Torino 10125, Italy*

Elena Cariati − *Department of Chemistry, University of Milano, Milano 20133, Italy;* orcid.org/0000-0003-1781-0360

Alma Cioci − *Department of Chemistry, University of Torino, Torino 10125, Italy*

Leonardo Lo Presti − *Department of Chemistry, University of Milano, Milano 20133, Italy; Laboratori Nazionali di Frascati, Istituto Nazionale di Fisica Nucleare (INFN), Frascati 00044, Italy;* orcid.org/0000-0001-6361-477X

Complete contact information is available at: https://pubs.acs.org/10.1021/acs.cgd.2c00560

Notes

The authors declare no competing financial interest.

■ ACKNOWLEDGMENTS

Financial support from MIUR (Ministero dell'Istruzione, dell'Università e della Ricerca) and Fondazione CRT is acknowledged.

■ REFERENCES

(1) Boyd, R. W. *Nonlinear Optics*; Academic Press−An imprint of Elsevier Science: San Diego, USA. 2003, ISBN: 0−12−121682−9.

(2) Dempsey, W. P.; Fraser, S. E.; Pantazis, P. SHG nanoprobes: Advancing harmonic imaging in biology. *BioEssays* **2012**, *34*, 351−360.

(3) Huang, X.; El-Sayed, I. H.; Qian, W.; El-Sayedet, M. A. Cancer Cell Imaging and Photothermal Therapy in the Near-Infrared Region by Using Gold Nanorods. *J. Am. Chem. Soc.* **2006**, *128*, 2115−2120.

(4) Jin, Y. Engineering Plasmonic Gold Nanostructures and Metamaterials for Biosensing and Nanomedicine. *Adv. Mater.* **2012**, *24*, 5153−5165.

(5) Liu, T.-M.; Conde, J.; Lipiński, T.; Bednarkiewicz, A.; Huang, C.-C. Smart NIR linear and nonlinear optical nanomaterials for cancer theranostics: Prospects in photomedicine. *Prog. Mater. Sci.* **2017**, *88*, 89−135.

(6) Franken, P. A.; Hill, A. E.; Peters, C. W.; Weinreich, G. Generation of Optical Harmonics. *Phys. Rev. Lett.* **1961**, *7*, 118−119.

(7) Clevers, S.; Burel, A.; Couvrat, N.; Dupray, V.; Coquerel, G. Relevance of Second Harmonic Generation Microscopy (SHG-M) in Material Sciences *BIWIC 2019 International Workshop on Industrial Crystallization*; Rayong, Thailand. 2019, hal-02295938, https://hal-normandie-univ.archives-ouvertes.fr/hal-02295938.

(8) *CrysAlisPro*; Agilent Technologies, Version 1.171.37.31 (release 14-01-2014 CrysAlis171.NET), (2014, *18*: 38: 05).

(9) Sheldrick, G. M. SHELXT-Integrated Space-Group and Crystal-Structure Determination. *Acta Crystallogr. A Found. Adv.* **2015**, *71*, 3−8.

(10) Sheldrick, G. M. Crystal Structure Refinement with SHELXL. *Acta Crystallogr. C Struct. Chem.* **2015**, *71*, 3−8.

(11) Dolomanov, O. V.; Bourhis, L. J.; Gildea, R. J.; Howard, J. A. K.; Puschmann, H. OLEX2: A Complete Structure Solution, Refinement and Analysis Program. *J. Appl. Crystallogr.* **2009**, *42*, 339−341.

(12) Frisch, M.J.; Trucks, G.W.; Schlegel, H.B.; Scuseria, G.E.; Robb, M.A.; Cheeseman, J.R.; Scalmani, G.; Barone, V.; Petersson, G.A.; Nakatsuji, H.; Li, X.; Caricato, M.; Marenich, A. V.; Bloino, J.; Janesko, B. G.; Gomperts, R.; Mennucci, B.; Hratchian, H. P.; Ortiz, J. V.; Izmaylov, A. F.; Sonnenberg, J. L.; Williams-Young, D.; Ding, F.; Lipparini, F.; Egidi, F.; Goings, J.; Peng, B.; Petrone, A.; Henderson, T.; Ranasinghe, D.; Zakrzewski, V. G.; Gao, J.; Rega, N.; Zheng, G.; Liang, W.; Hada, M.; Ehara, M.; Toyota, K.; Fukuda, R.; Hasegawa, J.; Ishida, M.; Nakajima, T.; Honda, Y.; Kitao, O.; Nakai, H.; Vreven, T.; Throssell, K.; Montgomery, J. A., Jr.; Peralta, J. E.; Ogliaro, F.; Bearpark, M. J.; Heyd, J. J.; Brothers, E. N.; Kudin, K. N.; Staroverov, V. N.; Keith, T. A.; Kobayashi, R.; Normand, J.; Raghavachari, K.; Rendell, A. P.; Burant, J. C.; Iyengar, S. S.; Tomasi, J.; Cossi, M.; Millam, J. M.; Klene, M.; Adamo, C.; Cammi, R.; Ochterski, J. W.; Martin, R. L.; Morokuma, K.; Farkas, O.; Foresman, J. B.; Fox, D. J. *Gaussian 16, Revision C.01*; Gaussian, Inc.: Wallingford CT, USA, 2016.

(13) Schlegel, H. B.; Daudel, C. *Computational Theoretical Organic Chemistry*; Reidel Publ. Co. 1981.

(14) Schlegel, H. B. An efficient algorithm for calculating *ab initio* energy gradients using *s*, *p* Cartesian Gaussians. *J. Chem. Phys.* **1982**, *77*, 3676−3681.

(15) Schlegel, H. B. Optimization of equilibrium geometries and transition structures. *J. Comput. Chem.* **1982**, *3*, 214−218.

(16) Schlegel, H. B.; Binkley, J. S.; Pople, J. A. First and second derivatives of two electron integrals over Cartesian Gaussians using Rys polynomials. *J. Chem. Phys* **1984**, *80*, 1976−1981.

(17) Becke, A. D. Density-functional exchange-energy approximation with correct asymptotic behavior. *Phys. Rev. A Gen. Phys.* **1988**, *38*, 3098−3100.

(18) Becke, A. D. Density-functional thermochemistry. III. The role of exact exchange. *J. Chem. Phys.* **1993**, *98*, 5648−5652.

(19) Hehre, W.J.; Radom, L.; Schleyer, P. v. R.; Pople, J.A. *Ab initio Molecular Orbital Theory*; Wiley: New York, 1986.

(20) Wadt, W. R.; Hay, P. J. *Ab initio* effective core potentials for molecular calculations. Potentials for the transition metal atoms Sc to Hg. *J. Chem. Phys.* **1985**, *82*, 270−283.

(21) Hill, J. G.; Peterson, K. A. Gaussian basis sets for use in correlated molecular calculations. XI. Pseudopotential-based and all-electron relativistic basis sets for alkali metal (K−Fr) and alkaline earth (Ca−Ra) elements. *J Chem. Phys.* **2017**, *147*, 244106.
(22) Lim, I. S.; Stoll, H.; Schwerdtfeger, P. Relativistic small-core energy-consistent pseudopotentials for the alkaline-earth elements from Ca to Ra. *J. Chem. Phys.* **2006**, *124*, No. 034107.
(23) Parsons, D. F.; Ninham, B. W. Ab initio molar volumes and Gaussian radii. *J. Phys. Chem. A* **2009**, *113*, 1141−1150.
(24) Dovesi, R.; Saunders, V. R.; Roetti, C.; Orlando, R.; Zicovich-Wilson, C. M.; Pascale, F.; Civalleri, B.; Doll, K.; Harrison, N. M.; Bush, I. J.; D'Arco, P.; Llunell, M.; Causà, M.; Noël, Y.; Maschio, L.; Erba, A.; Rerat, M.; Casassa, S. *CRYSTAL17 User's Manual*; (University of Torino: Torino, 2017), https://www.crystal.unito.it/Manuals/crystal17.pdf.
(25) Dovesi, R.; Erba, A.; Orlando, R.; Zicovich-Wilson, C. M.; Civalleri, B.; Maschio, L.; Rerat, M.; Casassa, S.; Baima, J.; Salustro, S.; Kirtman, B. WIREs Quantum-mechanical condensed matter simulations with CRYSTAL. *WIREs Comput. Mol. Sci.* **2018**, *8*, e1360−e1396.
(26) Bourhill, G.; Mansour, K.; Perry, K. J.; Khundkar, L.; Sleva, E. T.; Kern, R.; Perry, J. W.; Williams, I. D.; Kurtz, S. K. Powder second harmonic generation efficiencies of saccharide materials. *Chem. Mater.* **1993**, *5*, 802−808.
(27) Marabello, D.; Antoniotti, P.; Benzi, P.; Canepa, C.; Diana, E.; Operti, L.; Mortati, L.; Sassi, M. P. Non-linear optical properties of β-D-fructopyranose calcium chloride MOFs: an experimental and theoretical approach. *J. Mater. Sci.* **2015**, *50*, 4330−4341.
(28) Ferrero, M.; Rérat, M.; Kirtman, B.; Dovesi, R. Calculation of first and second static hyperpolarizabilities of one- to three-dimensional periodic compounds. Implementation in the CRYSTAL code. *J. Chem. Phys.* **2008a**, *129*, 244110.
(29) Ferrero, M.; Rérat, M.; Orlando, R.; Dovesi, R. Coupled perturbed Hartree-Fock for periodic systems: the role of symmetry and related computational aspects. *J. Chem. Phys.* **2008b**, *128*, No. 014110.
(30) Ferrero, M.; Rérat, M.; Orlando, R.; Dovesi, R. The calculation of static polarizabilities of 1-3D periodic compounds. the implementation in the crystal code. *J. Comput. Chem.* **2008c**, *29*, 1450−1459.
(31) Kurtz, S. K.; Perry, T. T. A Powder Technique for the Evaluation of Nonlinear Optical Materials. *J. Appl. Phys.* **1968**, *39*, 3798−3813.
(32) Del-Corso, A.; Cappiello, M.; Moschini, R.; Balestri, F.; Mura, U.; Ipata, P. L. The furanosidic scaffold of d-ribose: a milestone for cell life. *Biochem. Soc. Trans.* **2019**, *47*, 1931−1940.
(33) Hu, H.; Xue, J.; Wen, X.; Li, W.; Zhang, C.; Yang, L.; Xu, Y.; Zhao, G.; Bu, X.; Liu, K.; Chen, J.; Wu, J. Sugar-metal ion interactions: the complicated coordination structures of caesium ion with D-ribose and myo-inositol. *Inorg. Chem.* **2013**, *52*, 13132−13145.
(34) Marabello, D.; Antoniotti, P.; Benzi, P.; Canepa, C.; Mortati, L.; Sassi, M. P. Synthesis, structure and NLO properties of new isostructural β-D-fructopyranose alkaline halide MOFs: a theoretical and experimental study. *Acta Crystallogr. B Struct. Sci. Cryst. Eng. Mater.* **2017**, *B73*, 737−743.
(35) Boyd, R. W. *Nonlinear Optics*, 3rd ed.; Academic Press: Philadelphia, 2008, ISBN:978-0-12-369470-6.
(36) Choudhury, R. R.; Chitra, R. Investigation of hydrogen bond effects on the hyperpolarizability of 2-Aminopyridinium maleate (2APM) complex and determining the non-linear optical susceptibility of the molecular crystal of 2APM. *Mol. Phys.* **2011**, *109*, 1701−1708.
(37) Marabello, D.; Antoniotti, P.; Benzi, P.; Beccari, F.; Canepa, C.; Cariati, E.; Cioci, A.; Lo Presti, L. Crystal structure or chemical composition of salt−sugar-based metal−organic frameworks: what are the nonlinear optical properties due to? *Acta Crystallogr. B Struct. Sci. Cryst. Eng. Mater.* **2021**, *77*, 506−514.
(38) Marabello, D.; Antoniotti, P.; Benzi, P.; Cariati, E.; Lo Presti, L.; Canepa, C. Developing new SrI2 and β-D-fructopyranose-based metal−organic frameworks with nonlinear optical properties. *Acta Crystallogr. B Struct. Sci. Cryst. Eng. Mater.* **2019**, *B75*, 210−218.
(39) Marabello, D.; Antoniotti, P.; Benzi, P.; Beccari, F.; Canepa, C.; Barge, A.; Boscaro, V.; Gallicchio, M.; Peira, E. Synthesis, Characterization and Cell Uptake of Nanoparticles for a Novel Approach to Radionuclide therapy: a Feasibility Study. *Int. J. Res. Pharm. Nano Sci.* **2019**, *8*, 230−240.
(40) Gavezzotti, A.; Lo Presti, L. Building Blocks of Crystal Engineering: A Large-Database Study of the Intermolecular Approach between C−H Donor Groups and O, N, Cl, or F Acceptors in Organic Crystals. *Cryst. Growth Des.* **2016**, *16*, 2952−2962.
(41) Lo Presti, L.; Pifferi, V.; Di Liberto, G.; Cappelletti, G.; Falciola, L.; Cerrato, G.; Ceotto, M. Direct measurement and modeling of spontaneous charge migration across anatase−brookite nanoheterojunctions. *J. Mater. Chem. A* **2021**, *9*, 7782−7790.
(42) Miller, T. M.; Bederson, B. Atomic and Molecular Polarizabilities-A Review of Recent Advances. *Adv. At. Mol. Phys.* **1978**, *13*, 1−55.
(43) Kaiser, H. F. The varimax criterion for analytic rotation in factor analysis. *Psychometrika* **1958**, *23*, 187−200.
(44) Rakotomalala, R. TANAGRA: un logiciel gratuit pour l'enseignement et la recherche *Actes de EGC'2005*; RNTI-E-3, 2005, *2*, 697−702, https://eric.univ-lyon2.fr/%7Ericco/tanagra/en/tanagra.html.

https://doi.org/10.1021/acs.cgd.2c00560
Cryst. Growth Des. 2022, 22, 5923−5934